Preparation of Graphene Oxide-loaded Nickel with Excellent Antibacterial Property by Magnetic Field-Assisted Scanning Jet Electrodeposition

Guibin Lou[1,2†], Ya Chen[1†], Junwei Xu[1], Yingjuan Qian[3], Haixia Cheng[1], Zhen Wei[4], Youwen Yang[5]*, Lida Shen[1,2]*, Cijun Shuai[6]

[1]College of Mechanical and Electrical Engineering, Nanjing University of Aeronautics and Astronautics, Nanjing 210016, China
[2]Key Laboratory of Digital Medical Equipment Technology of Jiangsu Province, Nanjing 210016, China
[3]MOE Joint International Research Laboratory of Animal Health and Food Safety, College of Veterinary Medicine, Nanjing Agricultural University, Nanjing, 210095 China
[4]Jiangsu Pharmaceutical Association, Nanjing 210016, China
[5] Jiangxi University of Science and Technology, Ganzhou 341000, China
[6]State Key Laboratory of High Performance Complex Manufacturing, Central South University, Changsha 410083, China
[†]*These authors contributed equally to this work*

Abstract: Graphene oxide (GO) is recognized as a promising antibacterial material that is expected to be used to prepare a new generation of high-efficiency antibacterial coatings. The propensity of GO to agglomeration makes it difficult to apply it effectively. A new method of preparing GO-loaded nickel (GNC) with excellent antibacterial property is proposed in this paper. In this work, GNC was prepared on a titanium sheet by magnetic field-assisted scanning jet electrodeposition. The massive introduction of GO on the coating was proven by energy disperse spectroscopy and Raman spectroscopy. The antibacterial performance of GNC was proven by agar plate assessment and cell living/dead staining. The detection of intracellular reactive oxygen species (ROS) and the concentration of nickel ions, indicate that the antibacterial property of GNC are not entirely derived from the nickel ions released by the coating and the intracellular ROS induced by nickel ions, but rather are due to the synergistic effect of nickel ions and GO.

Keywords: Graphene oxide; Antibacterial coating; Jet electrodeposition; Nickel

*Correspondence to: Lida Shen, College of Mechanical and Electrical Engineering, Nanjing University of Aeronautics and Astronautics, 29 Yudao Street, Nanjing 210016, China; ldshen@nuaa.edu.cn; Youwen Yang, Jiangxi University of Science and Technology, Ganzhou 341000, China; yangyouwen@csu.edu.cn

1. Introduction

Microbial safety has attracted intense research interest worldwide. Bacteria are widely distributed in nature, and many can attach to the surface to form biofilms, posing a constant threat to human health and economy[1]. The prevention of bacterial colonization and infection in human daily life and the working environment is extremely important to human health. In addition, biofilm will also reduce or even fully destroy the functional performance of surfaces, for example, in ships, petroleum pipeline metal structures, and medical implants[2-4]. Antibacterial coatings have been mainly achieved using three major strategies[5] of contact-killing, antibacterial agent release and anti-adhesion/bacteria-repellence[6-10]. At present, there is an increasing demand for improved performance of antibacterial surfaces in terms of environmental friendliness, reliability, and efficiency. Thus, the development of a new generation of safe,

reliable, and durable antibacterial coatings is increasingly urgent.

Nickel is widely used in coatings to protect metal substrates from corrosion due to its good corrosion resistance and wear resistance[11]. Antibacterial coatings with excellent comprehensive properties are expected to be obtained through the preparation of nickel-based composite coatings. As a derivative of graphene, graphene oxide (GO) is obtained by oxidation of graphite under acidic conditions[12]. Due to its unique physical and chemical properties, GO has important research value in biology, energy, medicine, sensors, and other fields[13-15]. Abundant oxygen-containing functional groups are distributed on the edge (hydroxyl and carboxyl) and base surface (epoxy) of GO sheets, endowing GO with excellent hydrophilicity, and dispersibility[16]. Since GO was first reported to exhibit antibacterial ability in 2010[17], many studies on the antibacterial mechanism and application of GO have begun to be carried out. The physical damage of the sharp edges of GO, the effect of oxidative stress, and wrapping or trapping of bacterial membranes by the thin film of GO are considered to be the three mainstream antibacterial mechanisms of GO[18-20]. In addition, theories regarding the extraction of lipid bilayers and the interference of signal proteins have been reported[21,22]. Although the antibacterial mechanism of GO is still controversial, the outstanding antibacterial performance of GO has been accepted, and its applications are being expanded. Some methods for the preparation of GO coatings have been reported, such as cold spraying, thin evaporation, chemical vapor deposition, electrophoretic deposition, and chemical grafting[23-25].

Additive manufacturing (AM), defined as a process to build three-dimensional (3D) objects by joining materials layer by layer, has been used in automotive, aerospace, printed electronics, and healthcare[26-30]. Inkjet printing and electrohydrodynamic jetting are widely used in printed electronics and biological printing with their excellent dimensional accuracy[31-34]. Compared with the traditional coating process, AM can shorten the production cycle of coating preparation, does not require assembly or mold preparation, and consumes less energy[35]. Laser melting deposition is an efficient method that can effectively enhance the fusion of powder and matrix and is widely used in the preparation of ceramic-reinforced metal-based composite coatings[27,36]. As a kind of AM technology, local electrochemical deposition technology can realize the directional deposition of metal ions layer by layer to print metal parts[37]. In the process of jet electrodeposition, the pumped plating bath forms a conductive jet between the cathode and anode under the restriction of the nozzle, and the deposition is realized in the contact area between the jet and the cathode. By adjusting the position of the deposition area on the surface

of the cathode, a variety of patterns can be obtained. The metal plating layer deposited in the previous step can be used as the substrate for the next deposited layer. As the number of reciprocating scans of the deposition area increases, the coating grows layer by layer, forming a three-dimensional geometric entity. The high efficiency mass transfer of the jet between the electrodes makes the jet electrodeposition have the advantage of high limit current, which is conducive to the improvement of the coating deposition efficiency and the enhancement of the bonding force with the substrate[38,39]. By adjusting the composition of the plating bath, multiple composite coatings can be prepared. The flowing plating bath will promote the dispersion of the second phase in the bath and improve the uniformity of the composite coating, and no additional post-process is required after the coating is prepared. Therefore, jet electrodeposition is widely used for the preparation of composite coatings[38,40].

However, the agglomeration of GO in the plating bath has always been a challenge for the preparation of GO composite coating. The agglomerates of GO in the plating bath will have a great negative impact on the preparation of the coating. It is also common that GO cannot be introduced into the coating due to agglomeration (**Figure S1**). To solve the problem of the difficulty of the deposition of GO on the coating, the magnetic field-assisted scanning electrodeposition technique was applied to the fabrication of GO-loaded nickel (GNC). Magnetic field-assisted jet electrodeposition is a new type of process for preparing composite coatings, and our group has reported the preparation of Nickel/Silicon Carbide (Ni-SiC) composite coating by magnetic field-assisted jet electrodeposition[41]. The introduction of magnetic field and ferromagnetic particles promoted the deposition of GO on the coating. In this work, GO is no longer independently dispersed into the plating bath as the second phase, but is dispersed into the plating bath together with ferromagnetic nickel particles (Nip). The sheet-like GO adsorbs on the surface of the Nip to form GO-loaded nickel particles. During the cathode deposition process, the permanent magnet under the cathode provides a stable magnetic field to capture the Nip. As the nickel coating grows, these GO-loaded particles are bound and fixed by the nickel coating, and eventually become part of the coating. In this work, the GNC was prepared by magnetic field-assisted scanning jet electrodeposition, and then the antibacterial activity and the antibacterial process of the composite coating were studied.

2. Materials and methods

2.1. Materials

GO used in the experiment is commercial few-layer GO purchased from Guoheng Technology Co., Ltd (China).

The ferromagnetic particles used in the experiment are reduced nickel powder purchased from Aladdin Co., Ltd (China), with an average particle size of 50 μm. Pure titanium sheets were used as the substrate with dimensions of 30 mm × 30 mm × 0.5 mm. The weak cytotoxicity of titanium is beneficial to reflect the antibacterial properties of the coating. Watts nickel bath was used as the basic plating bath. The composition of basic plating bath is shown in **Table 1**. All experimental reagents were analytical grade and distilled water was used to prepare the plating bath.

2.2. Preparation of composite plating bath

To promote the dispersion of GO in the bath, the two-step dispersion method was adopted. In the first step of dispersion, GO powder and sodium dodecyl sulfate (SDS) were dispersed in distilled water at a ratio of 5 g/L and 0.5 g/L, respectively (**Figure 1A**). An ultrasonic oscillator with a power of 240 W was used. Ultrasonic treatment for 1 h was used to promote the uniform dispersion of GO. As an anionic additive, dissolved SDS can form an electrostatic balance with GO to maintain the dispersed state of GO[42]. While preparing GO dispersion, the reduction nickel powder was dispersed into the basic bath according to the amount of 2 g/L, accompanied by magnetic stirring and ultrasonic vibration for 1 h (**Figure 1B**). The Nip were evenly dispersed in the plating bath, after sufficient ultrasonic treatment. In

the second step of dispersion, the GO dispersion was gradually added to the bath containing Nip in a volume ratio of 1:9 (**Figure 1C**). The plating bath is titrated to control the concentration of GO in the composite plating bath to 0.5 g/L, and the whole process was carried out under the conditions of magnetic stirring and ultrasonic vibration for 1 h, so that the GO can be uniformly mixed with Nip and fully contacted. Finally, GO and Nip adsorb each other and stably dispersed in the composite plating bath (**Figure S3**).

2.3. Preparation of the GNC

The titanium sheets were polished and cleaned with acetone and alcohol, and finally were cleaned ultrasonically with distilled water. The plating bath is kept at 40℃ and is circulated and pumped by a water pump, and the flow rate of the bath at the nozzle is maintained at 200 L/h. **Figure 2A** illustrates the experimental device. The flowing plating bath will accumulate in the anode cavity under the action of the pump and is sprayed onto the cathode substrate through a rectangular nozzle. The flowing plating bath connects the cathode and anode and forms a jet between the electrodes. The distance between the nozzle and the cathode substrate is maintained at 2 mm. The nickel rod in the anode tube is used as a soluble electrode to supplement the consumed nickel ions. The jet between the electrodes is excited by a current of 100 A/dm^2, and the nickel coating is deposited on the surface of the cathode below the nozzle. A large-area permanent magnet placed 3mm below the cathodes provides a uniform magnetic field with a strength of 100 mT to capture the Nip in the jet. In the deposition process, the deposition area of nickel ions is focused on the impact area of the jet on the cathode under the restriction of the nozzle. The anode and nozzle will perform a reciprocating uniform scanning movement

Table 1. Compositions of basic plating bath.

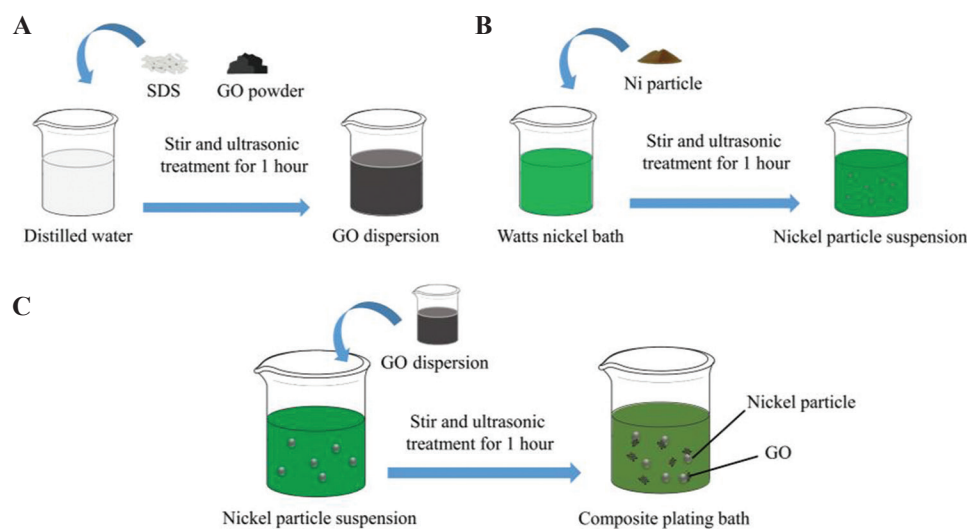| Bath composition	Content
$NiSO_4 \cdot 6H_2O$	260 g/L
$NiCl_2 \cdot 6H_2O$	40 g/L
H_3BO_3	40 g/L
Saccharin	5 g/L

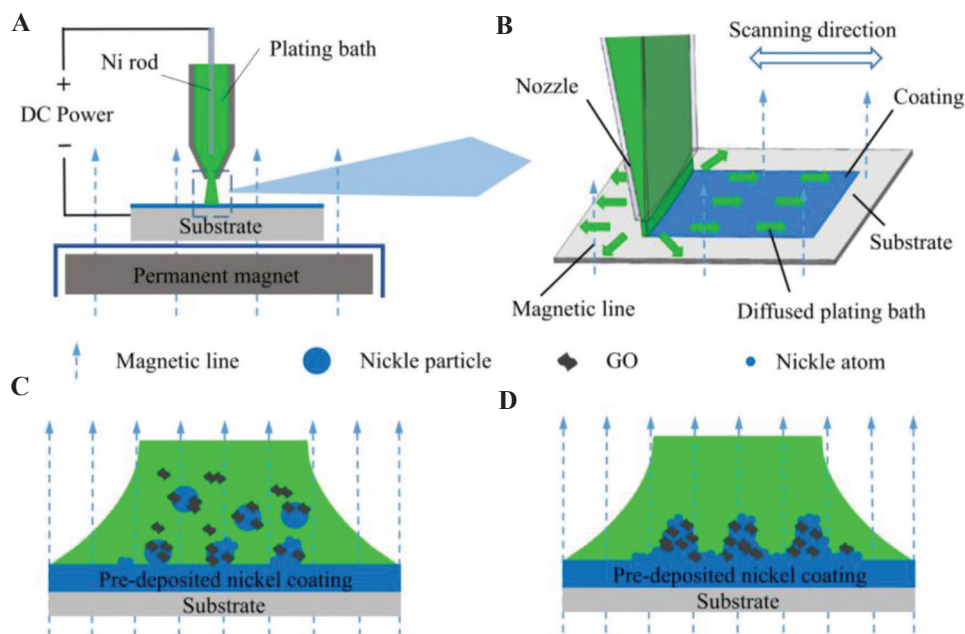**Figure 1.** (A-C) Schematic of preparing the composite plating bath.

Figure 2. (A) Schematic diagram of experimental equipment. (B) The process of composite coating. (C-D) Model of introducing GO into the coating.

(4 mm/s) in the horizontal direction relative to the fixed substrate along the designed path provided by the model file (**Figure 2B**). As the number of reciprocating scans increases, the thickness of the coating increases layer by layer, and finally a three-dimensional geometric model is formed. The size of the scanning area is 20 × 20 mm². The jet from the nozzle hit the surface of the cathode and spread around, and the diffused plating bath was collected by the external container and reused. In the initial stage of deposition, the nickel ions were reduced at the cathode to form a pre-deposited nickel coating. At the same time, a large number of Nip also impact the surface of the cathode along with the jet. Under the action of an external magnetic field, the pre-deposited nickel coating and the ferromagnetic Nip were simultaneously magnetized to generate opposite magnetic poles. The Nip are attracted to the surface of the cathode nickel coating along the magnetic line of induction[41,43]. A part of the Nip will be transferred out of the cathode surface under the impact of the jet, and the remaining part of the Nip can come into contact with the nickel coating. The exposed area of the Nip surface (not covered by GO) can be used as a site for combine with the nickel coating (**Figure 2C**). The Nip combined with the coating to form strong adsorption. At high current density, a large amount of nickel ions are deposited on the surface of the cathode. The growing coating wraps and fixes these particles in the coating to obtain a GNC (**Figure 2D**).

To evaluate the influence of nickel plating and Nip on the antibacterial activity of samples, the coating prepared with traditional Watts nickel bath was named

Table 2. Each sample corresponds to the additive phase in the plating bath.

Sample	WNC	PNC	GNC
Nickel particles (g/L)	0	2	2
Graphene oxide (g/L)	0	0	0.5

WNC and the coating prepared with Watts nickel bath added with Nip was named PNC. The list of samples is shown in **Table 2**. The deposition time for each sample is 30 min. In addition, a pure titanium sample (TI) was set to evaluate the influence of the substrate. The magnetic field only used to promote the doping of Nip carrying GO during the preparation process of the coating. In the absence of a magnetic field, Nip and GO cannot be effectively deposited on the cathode surface (**Figure S4**). In the subsequent antibacterial test, there was no difference between the failed coating and the pure nickel coating prepared by Watts nickel bath. Thus, the coatings prepared without a magnetic field have not been discussed.

2.4. Surface characterization

Surface morphologies of the coating on the samples were observed using a field emission scanning electron microscope (Hitachi Instruments, S-4800, Japan) equipped with an energy dispersive spectrometer (EDS) to examine the chemical composition. Raman microscopy was used to observe the Raman spectra of the GO powder and GNC using a laser wavelength of 532 nm (Thermo Fisher Scientific, DXR 2X, USA).

2.5. Antibacterial activity assessment

The antibacterial activity was assessed by agar plate assessment, and cell live/dead staining was used to directly observe whether the bacteria were alive or dead. *Escherichia coli* (*E. coli*, ATCC25922) and *Staphylococcus aureus* (*S. aureus*, ATCC25923) were used in this experiment. Luria-Broth was used for bacterial culture. Prior the experiment, a single colony of bacteria was added into the LB broth and cultivated overnight using a constant temperature shaker (220 rpm, 37℃) to obtain a bacterial solution for testing. Glass without antibacterial activity was used as a blank control sample, and the samples were disinfected with 75% ethanol for 30 min.

In agar plate assessment, the bacterial culture solution was diluted to ~1×10^6 CFU/mL with phosphate buffer solution (PBS). Bacterial suspension (100 μL) was inoculated on the samples and incubated at 37℃ for 2 h. After incubation, the samples were soaked in PBS (30 mL), and shaken using a shaker (220 rpm) for 10 min to rinse and collect the bacteria on the surfaces of the samples. Subsequently, the samples flushing liquid (100 μL) was introduced to the LB agar culture plate and cultured for 24 h.

For cell live/dead staining, bacterial suspension (100 μL) with a cell density of $2 - 3 \times 10^9$ CFU/mL was inoculated on the samples and incubated for 2 h at 37℃. Such a high concentration of bacteria is helpful for observation under a fluorescence microscope. After the incubation, the bacteria on the samples were stained with cell live/dead kit containing 4', 6-diamidino-2-phenylindole (DAPI) and propidium iodide (PI), and then incubated for 15 min in the dark at 37℃. DAPI can pass through intact cell membranes and bind to bacterial DNA. All of the bacteria were stained with DAPI and fluoresced blue, while only cells with damaged membranes can be stained as red by PI. Subsequently, PBS (200 μL) was used to rinse excess stain. Finally, a laser microscope (Olympus, IX83, Japan) was used to observe the experimental result.

2.6. Intracellular reactive oxygen species (ROS) assay

2', 7'-dichlorodihydrofluorescein diacetate (DCFH-DA) was used to investigate the intracellular ROS levels in the bacteria collected from the samples. DCFH-DA can be transformed into non-fluorescent DCFH by intracellular esterase and DCFH can be oxidized by ROS into fluorescent DCF. Because the incubation time of the bacteria on the surface of samples is within 2 h, to record the accumulation of intracellular ROS, DCFH-DA 10 μM is dispersed in the bacterial suspension in advance when the bacteria are inoculated on the surface of the samples.

The bacterial suspension was diluted to 10^6 CFU/mL. After the incubation, the bacteria on the samples were collected by PBS (2000 μL). A fluorescence microplate reader (Tecan Infinite, 200Pro, Switzerland) was used to quantitatively determine the intracellular ROS level of bacteria in PBS. The excitation light wavelength was set to 488 nm.

2.7. Measurement of nickel ion release

The nickel ion releasing ability of the samples was detected, and PBS was used to simulate the living environment of the bacteria. Samples were immersed in PBS (10 mL) for 2 h at 37℃. The concentration of nickel ions in the resultant solution was determined by inductively coupled plasma mass spectroscopy (Agilent, Agilent 7700/7800, USA).

3. Results and discussion

3.1. Surface characterizations of the samples

Figure 3A shows the photos of the samples. The uncoated substrate and the WNC possess a shiny surface. The introduction of Nip and a magnetic field caused the GNC and PNC to be darkened. Under the effect of GO in the plating bath, the surface of GNC is darker than PNC. Raman spectroscopy is commonly used to characterize GO. In the Raman spectrum of the GO, the peaks at 1356 cm^{-1} corresponding to D band due to the edges and defects and 1611 cm^{-1} corresponds to the G band, depicting the in-plane stretching vibrations of C-sp^2 atoms[44]. The D and G peaks of GO can be clearly observed on the Raman spectrum of GNC, but no characteristic peaks of GO can be found on WNC and PNC (**Figure 3B**). The presence of the D and G peaks in the Raman spectrum confirms the existence of GO on the surface of GNC[45].

Figure 3C shows a typical morphology of nickel coating with large grains and cellular bulges. Observed under high magnification, the surface of the WNC is flat and dense. WNC is prepared by the traditional Watts nickel bath, so WNC possess a low surface roughness. However, due to the introduction of Nip and a magnetic field, a large number of coral-like clusters on the surface of the PNC were observed (**Figure 3D**). This unique morphology appear due to the external magnetic field trapping the ferromagnetic Nip in the bath and the mutual repulsive magnetic force existing between the adjacent clusters[40]. According to the principle of minimum energy, the distribution of particles along the lines of magnetic force has a tendency of peaking[46,47]. Affected by the tip effect, the electric field at the protrusion is more concentrated, the current density is higher, and the deposition speed is faster. Finally, coral-like clusters are formed on the coating. The gap between the protrusions is approximately 20 μm, and the surface roughness of the coating is greatly improved.
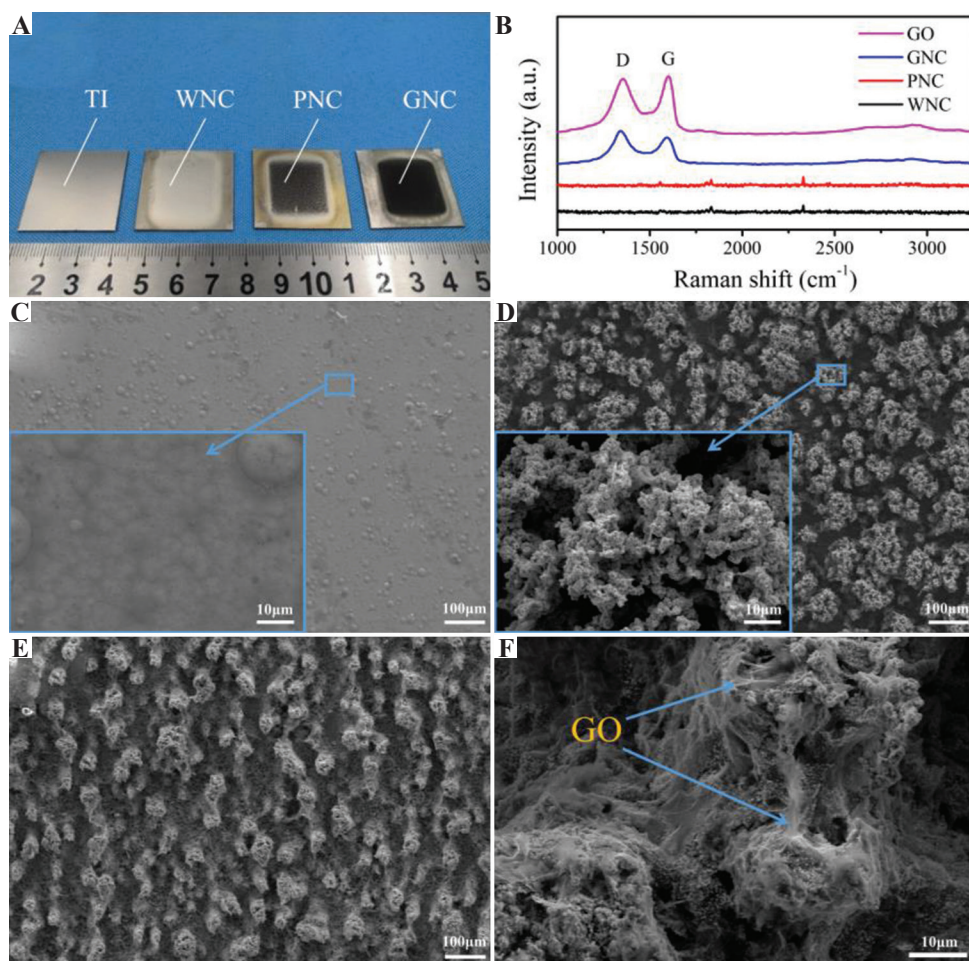
Figure 3. (A) Photos of samples. (B) Raman spectrum of graphene oxide and coated samples. The morphology of (C) WNC, (D) PNC, and (E-F) GNC.

Observed under high magnification, the coral-like clusters on the surface of the PNC are full of holes and the texture is very loose.

Similar to PNC, due to the influence of PNC and magnetic field, dense clusters are also distributed on the surface of the GNC (**Figure 3E**). The diameter of clusters on the surface of GNC is smaller than that of PNC, which is mainly affected by GO in the plating bath. Unlike PNC, the clusters on the surface of GNC are covered by a large amount of transparent sheet-like material (**Figure 3F**). The transparent sheet-like material is very consistent with the morphology of GO under the electron microscope. Similar phenomenon are reported in the co-deposition of copper-GO composites[48]. Combined with the results of Raman spectroscopy, it is confirmed that GO is heavily covered on the surface of GNC.

Figure 4A shows the EDS mapping images of the section of GNC. The cross section was previously polished and corroded by nitric acid. A large amount of transparent sheet-like material can be observed to fills the internal pores of the coating. Since GO is mainly composed of carbon and oxygen. The distribution area of the transparent material coincides with the main distribution area of carbon and oxygen, further confirming that the transparent GO was successfully introduced into the coating. The weight percentage of each element on the cross section is detected, as shown in **Figure 4B**. The weight percentage for carbon and oxygen on the cross section of GNC is 46.1% and 10.8%, respectively. The sample is corroded by dilute nitric acid and then repeatedly ultrasonically cleaned in deionized water. The drying and detection of the samples were carried out in the ultra-clean room. Such a high content of carbon mainly comes from the GO in the coating. The results of various tests show that massive GO material can be introduced into the coating by the method of magnetic field-assisted scanning jet electrodeposition, with the help of ferromagnetic particles carrying GO.

3.2. Assessment of antibacterial activity

The agar plate assessment was used to evaluate the antibacterial activity of the samples.

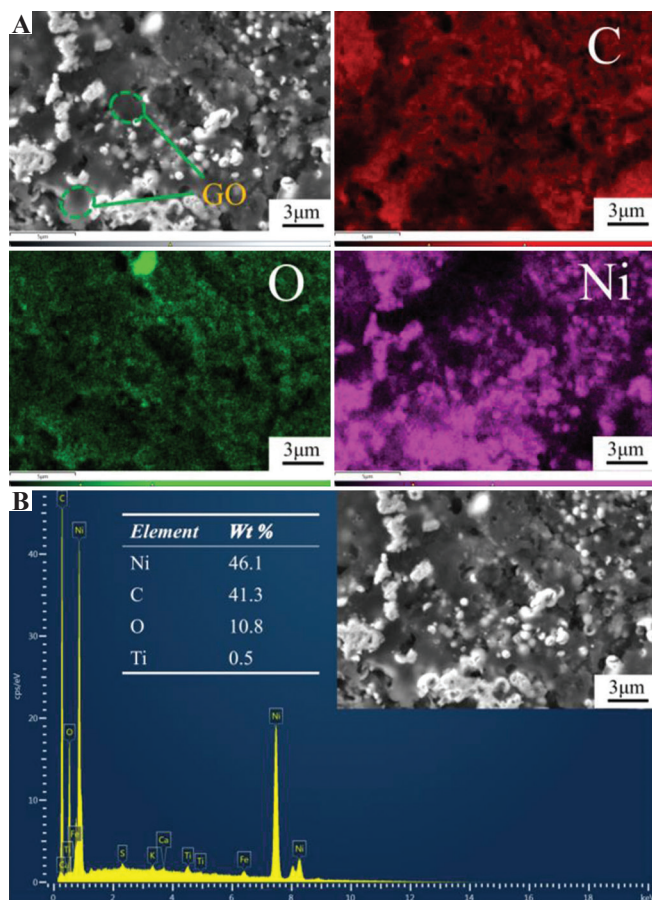The experimental results for *E. coli* are shown in **Figure 5A**. The survival rates of bacteria were counted after 1 and 2 h incubation to provide distinguishable results. For the blank control sample, the colonies were densely distributed on the agar plate. Only minor differences can be observed between the blank control sample and TI, indicating that TI only shows an insignificant antibacterial activity against *E. coli*, in agreement with the results obtained by Qiu *et al*.[49] WNC and PNC with nickel plating exhibit antibacterial properties. After 1 h of incubation on the surface of the samples, the cell viability of *E. coli* on the surface of WNC was only 71.1%, while that of PNC was 60.7%. After 2 h of incubation, the cell viability decreased further. At this time, the cell viability of *E. coli* on WNC and PNC were 53.7% and 35.4%, respectively. Nickel coating shows an obvious antibacterial effect on *E. coli* as shown by the comparison with TI and blank control sample, but there are still a large number of surviving bacteria on the surface of WNC and PNC. However, GNC showed a strong inhibitory effect on *E. coli* within 1 h, with a cell viability of 5% at 1 h. And this value was close to 0% at 2 h. The surface of the GNC exhibit highly effective antibacterial property against *E. coli* and can inactivate all bacteria within 2 h. This remarkable property is mainly related to the presence of GO materials on the coating. As shown in **Figure 5B**, the antibacterial activities of the samples against *E. coli* within 2 h can be expressed as GNC>PNC>WNC>TI.

The experimental results for *S. aureus* are shown in **Figure 5C**. The agar plate assessment result of *S. aureus* was similar to that for *E. coli*. As shown in **Figure 5D**, the antibacterial activities of the samples against *S. aureus* within 2 h can be expressed as GNC>PNC>WNC>TI. The difference from the results obtained by incubating *E. coli* is that WNC and PNC show a stronger bactericidal activity on *S. aureus*. After 2 h of incubation, the cell viability of *S. aureus* on WNC and PNC were only 35.4%
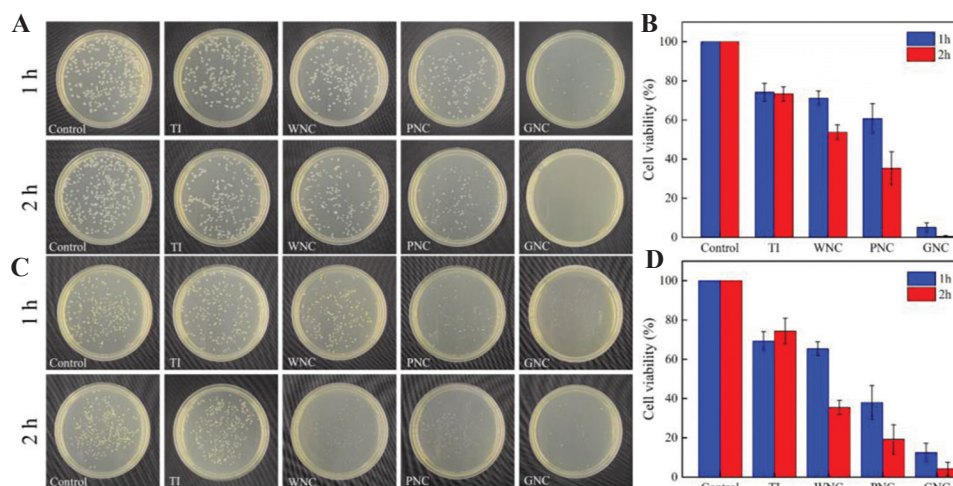

Figure 4. Energy dispersive spectrometer (EDS) analysis of the section of graphene oxide-loaded nickel. (A) The EDS mapping images of C, O, and Ni elements. (B) The weight percentage of each element.

Element	Wt %
Ni	46.1
C	41.3
O	10.8
Ti	0.5

Figure 5. Evaluation of antibacterial activity. (A) Incubate *Escherichia coli* on samples. (B) The cell viability of *E. coli* on the surface of samples. (C) Incubate *Staphylococcus aureus* on samples. (D) The cell viability of *S. aureus* on the surface of samples.

and 19.3%, respectively. In addition, although GNC also showed strong antibacterial effects against *S. aureus* within 2 h, some colonies were still present on the plate corresponding to GNC. Although *S. aureus* cannot be completely inactivated by GNC within 2 h, the average cell viability of *S. aureus* is <15% after 1 h incubation, and <5% after 2 h. The agar plate assessment showed that GNC possess rapid and excellent antibacterial activity against *S. aureus* and *E. coli* within 2 h.

3.3. Fluorescence staining of live/dead bacteria

Although the agar plate assessment is a classic method for the evaluation of the number of alive bacteria, the survival status of bacteria on the surface of samples cannot be directly observed using the method. The live/dead cell staining technique was used to directly distinguish live and dead bacteria on the surfaces of the samples. Both live and dead cells can be stained as blue by DAPI, whereas PI can only stain bacteria with broken membranes, that is, dead bacteria. Live/dead staining fluorescent images of *E. coli* are shown in **Figure 6A**. For the blank control sample and TI, strong blue fluorescence can be observed, and red fluorescence was almost invisible. A very small amount of red bacteria is only attributed to the normal metabolic death of bacteria. WNC and PNC all showed different degrees of antibacterial activity, because while more bacteria died on their surface than on the surface of the blank control sample, but a large number of *E. coli* still survived and
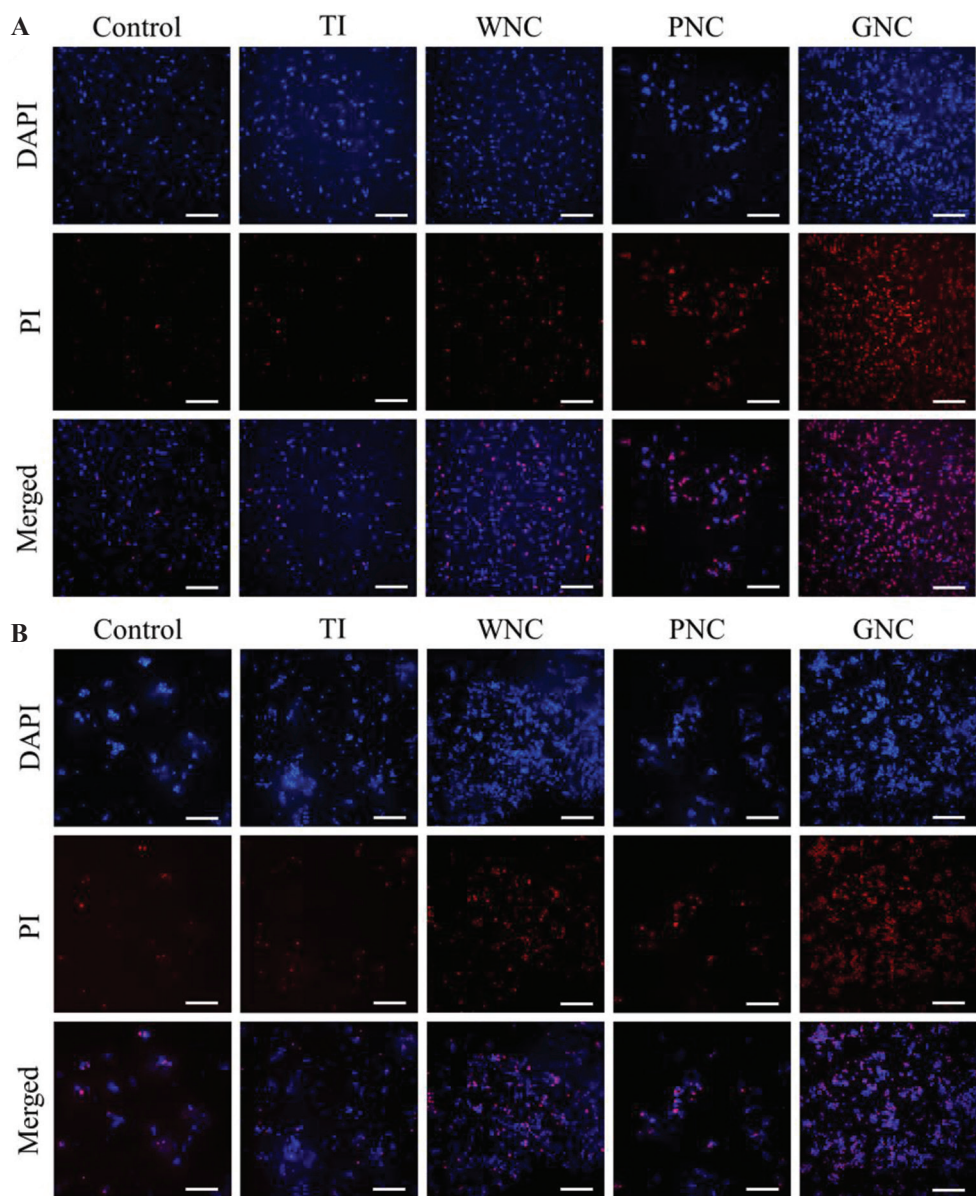

Figure 6. Live/dead staining fluorescent images of *Escherichia coli* and *Staphylococcus aureus*. (A) *E. coli* cells were inoculated on the sample surfaces and incubated for 2 h. (B) *S. aureus* cells were inoculated on the samples surfaces and incubated for 2 h. Scale bar: 20 μm.

were not stained as red by PI. However, almost all *E. coli* observed on the surface of GNC was stained as red by PI, implying that almost all *E. coli* died. Fluorescence images show that GNC can indeed effectively inactivate *E. coli* on its surface. The order of the antibacterial activity of the samples against *E. coli* is consistent with the agar plate assessment, and GNC has better antibacterial activity against *E. coli* than the other samples.

Similar results obtained for *S. aureus* are shown in **Figure 6B**. The ability of GNC to inactivate *S. aureus* is more significant compared with other samples. Most of *S. aureus* died on the surface of GNC. However, after the same incubation time, a small part of *S. aureus* was not stained red on the surface of GNC. This shows that the *S. aureus* has not been completely killed *S. aureus* has a higher cell viability on GNC, which may be due to that Gram-positive bacteria (*S. aureus*) have thicker cell walls compared to Gram-negative bacteria (*E. coli*). Combined with the results of the agar plate assessment, although the *S. aureus* on the surface of GNC was not completely stained as red, the cell vitality of *S. aureus* had been lost, and the remaining bacteria could not form dense colonies on the agar plate. It was concluded that GNC can be used as an effective antibacterial platform that causes severe membrane damage to bacteria and causes bacteria death.

3.4. Effect of ROS and nickel ions

As shown by the above experiments, WNC, PNC, and GNC all exhibit better antibacterial performance than TI. GO was not detected on the surface of WNC and PNC, so the antibacterial activity of WNC and PNC mainly comes from the metallic nickel of the coating. Due to the incomplete coverage of GO, the bare metallic nickel on the surface of GNC may also participate in the antibacterial process of GNC. Metal materials are widely used for antibacterial[50,51]. As a traditional inorganic bactericide method, metal ions have been reported to inactivate the oxidase involved in bacterial respiration and induce the production of ROS[52-55]. For GNC, few layers of GO were used in this experiment, and the GO on the surface of GNC shows a soft fibrous shape and

does not exhibit any sharp edges (**Figure 3F**). GO was anchored on the coating and does not appear to be a free state, so that the wrapping mechanism or physical cutting has a limited influence on the antibacterial activity. Since these effects are excluded as the origin of the bacterial activity of GO, the ROS dependent oxidative stress effect and electron transfer may be the antibacterial mechanism of GO on the surface of GNC[19,56-58].

To detect the level of ROS during the incubation of bacteria on the coated samples, DCFH-DA was used as an indicator of intracellular ROS, as shown in **Figure 7**. In the experiment of two types of bacteria, a low level of ROS was detected in the bacterial liquid recovered from the TI at the two detection points. Such a low level of ROS did not show an evident inhibitory effect on the bacteria, which is consistent with the results of antibacterial experiment. However, high levels of intracellular ROS were detected in WNC, PNC and GNC, indicating that the antibacterial ability of coated samples is related to the oxidative stress effect of intracellular ROS. The nickel ions released by the metallic nickel on the coating may induce the production of ROS. Nickel ions can cause cells to produce high levels of intracellular ROS, causing damage to cell lipids and DNA, decreasing intracellular enzyme activity and leading to cell apoptosis[59-61].

To further explore the relationship between the release of nickel ions from the samples and the level of ROS, an inductively coupled plasma mass spectrometer was used to detect the nickel ion release rate of the samples. To avoid interference from the culture medium and the metabolites of bacteria, the same amount of PBS (10 mL) was used to soak the coated samples to simulate the incubational environment of bacteria. The results for the concentration of nickel ions are shown in **Figure 8**. After immersing for 2 h, the concentration of nickel ions released by WNC was only 4.49 μg/mL, while the corresponding values for PNC and GNC were 10.43 μg/mL and 8.6 μg/mL, respectively. The highest concentration of nickel ions released from PNC was mainly due to the larger actual contact area between the rough surface of the PNC and the liquid that promoted the
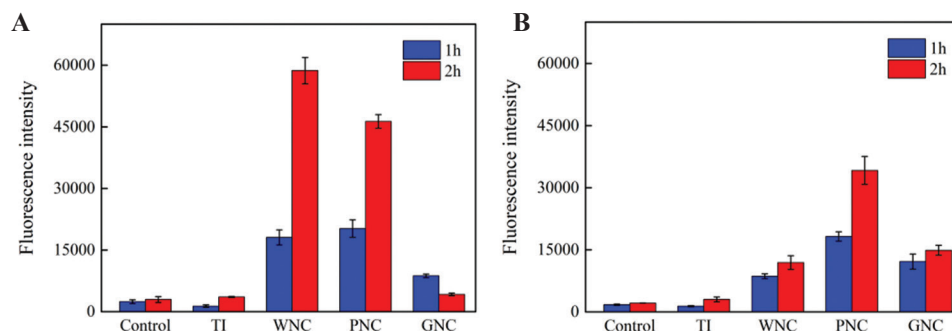

Figure 7. Quantitative analysis of the reactive oxygen species intensity. (A) *Escherichia coli*. (B) *Staphylococcus aureus*.

release of nickel ions. This explains why the antibacterial activity of PNC is better than that of WNC because PNC can produce a higher concentration of nickel ions around it. GNC and PNC have similar morphological characteristics, but the former released fewer nickel ions than the latter. This is mainly because the presence of GO on the surface of GNC hinders the release of nickel ions.

The nickel ion release rate of GNC is between PNC and GNC, but the level of ROS is significantly lower than that of PNC and WNC during the incubation period (**Figure 7**). Therefore, the excellent antibacterial activity of GNC cannot be explained by nickel ions and the intracellular ROS mediated by ions. In fact, the antibacterial effect of GNC was faster than those for WNC and PNC, and the sterilization is more thorough. The results of the agar plate experiment showed that the bacterial cell viability on GNC decreased significantly after 1 h of incubation (**Figure 5B and D**). At the same time, there are still a large number of surviving bacteria on the surface of WNC and PNC. For bacteria on GNC, the short survival time is insufficient to accumulate high level of intracellular ROS. The antibacterial performance of WNC and PNC in the agar plate assessment also shows that the antibacterial effect of nickel ions is a relatively slow process, and the fast-acting antibacterial ability of GNC was not entirely derived from nickel ions. It shows that the GO on GNC also participates in the antibacterial process, and the effect of GO on bacteria is more rapid, resulting in the antibacterial effect of nickel ions is not fully exerted.

3.5. Possible antibacterial mechanism

The GO coating prepared on the metal can form a GO-metal system with the metal matrix. The antibacterial properties of GO-metal systems have been widely reported[44,62]. In the environment of incubating bacteria, GO can act as a terminal electron acceptor in bacterial respiratory chain and extract electrons from microbial membranes, realizing the reduction of GO[63,64]. Panda *et al.*[65] studied the antibacterial properties of the GO-metal system and reported that the electron transport pathway can be interrupted by the GO-metal system and inhibit the metabolic process of bacteria, the functional groups exist on the surface and edges of GO that serve as sites for the generation of ROS after accepting electrons. Qiu *et al.*[49] prepared a GO coating on the surface of titanium, and also confirmed that the antibacterial ability of the coating comes from the electron transfer between the bacteria and the GO-metal system.

Since the coverage of GO on the surface of GNC is incomplete, the excellent antibacterial activity of GNC mainly comes from two aspects. On the one hand, the nickel ions released from the surface of GNC induce the generation of intracellular ROS in the bacterial cells,

following the same process as that for WNC and PNC. On the other hand, electron transfer occurs between GNC and bacteria, inhibiting or even interrupting the metabolic process of the bacteria[65]. The electrons accepted by GO mediate the generation of ROS on its oxygen-containing functional group[66], and some of the ROS will become intracellular ROS due to the internalization of bacteria[67,68]. The remaining part will be distributed around the bacteria as extracellular ROS, enhancing the oxidative stress on the bacteria. The strong oxidative stress effect increases the permeability of the cell membrane and leads to the penetration and destruction of the bacterial cell membrane.

The antibacterial process of GNC on bacteria is illustrated in **Figure 9**. In the initial stage of bacterial inoculation on the surface of GNC, GO exerts the main antibacterial effect, because of the low concentration of the nickel ions released on the surface of GNC (**Figure 9B**). Due to the non-oxidative electron transfer between GO and bacteria, the metabolism of the bacteria is severely inhibited by GO, resulting in decreased bacterial activity. Meanwhile, the ROS mediated by GO cause oxidative stress damage to bacteria. As the incubation time increases, nickel ions continue to accumulate around the bacteria. Since the effect of GO on bacteria is more rapid in the initial period, the function of nickel ions is not fully exerted. However, the high concentration of nickel ions further enhances the antibacterial effect of GNC by inducing the generation of ROS (**Figure 9C**). Finally, under the synergistic effect of nickel ions and GO (**Figure 9D**) inhibited respiration and oxidative stress lead to the death of bacteria. There are differences in the cell walls and outer membranes between Gram-negative and Gram-positive bacteria. *S. aureus* is an aerobic bacteria, and its final electron acceptor is oxygen rather than the extracellular environment, and a thicker cell wall makes
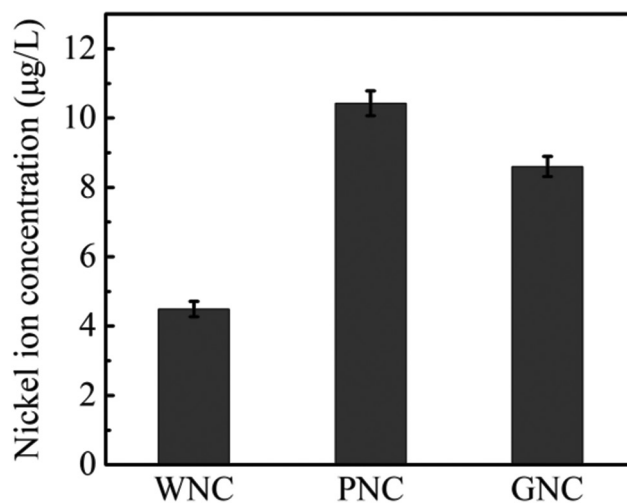

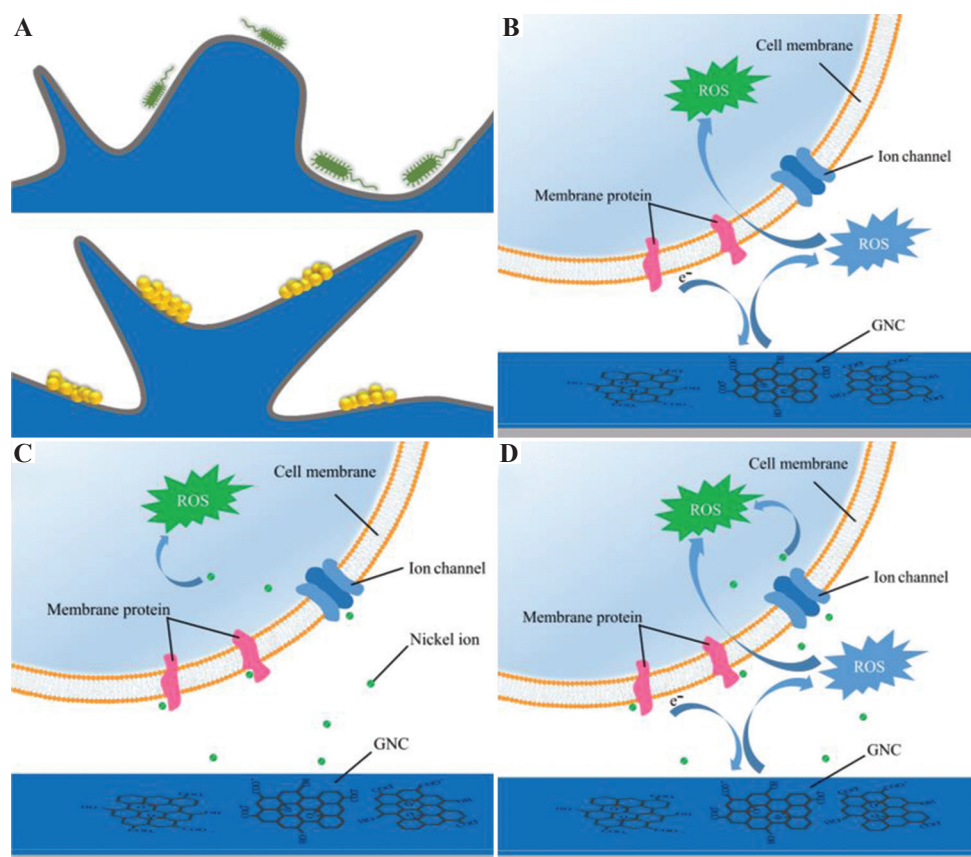**Figure 8.** Concentration of nickel ions released by the coated samples.

Figure 9. Schematic illustration of the possible antibacterial mechanism of graphene oxide (GO)-loaded nickel. (A) Contact of bacteria and coating. (B) Effect of GO on bacteria. (C) Effect of nickel ions on bacteria. (D) Synergistic effect of GO and nickel ions.

it difficult to carry out extracellular electron transfer[69,70]. As a result, the antibacterial effect of GO on *S. aureus* is relatively weak, so that *S. aureus* shows a higher cell viability on the surface of GNC than *E. coli*.

4. Conclusions

The ferromagnetic particle carrier method and the magnetic field-assisted scanning jet electrodeposition technique were applied to the fabrication of the GNC. A large amount of GO covered on the coating endows the coating with excellent antibacterial properties. The antibacterial rate of GNC against *S. aureus* exceeds 90% with 2 h and is close to 100% against *E. coli*. The presence of intracellular ROS was detected in the bacterial suspension collected on the surface of GNC. The antibacterial properties of GNC was not entirely derived from intracellular ROS mediated by nickel ions, but rather was the result of the synergistic effect of nickel ions and GO on the bacteria. The combination of GO and nickel realizes rapid sterilization and long-term antibacterial effect, respectively. GNC can be used as an effective antibacterial platform that induces the death of bacteria on its surface.

Conflict of interest

The authors declare no competing financial interest.

Author contributions

G.L. Conceptualization, methodology, software, writing - review & editing. Y.C. Reviewing and editing, methodology, data curation. J.X. Software. Y.Q. Investigation. H.C. Visualization. Z.W. Investigation. Y.Y. Supervision. L.S. Funding acquisition. C.S. Investigation.

References

1. Simoes M, Simoes LC, Vieira MJ, 2010, A Review of Current and Emergent Biofilm Control Strategies. *Lwt Food Sci*

Technol, 43:573–83.

https://doi.org/10.1016/j.lwt.2009.12.008

2. Pistone A, Scolaro C, Visco A, 2021, Mechanical Properties of Protective Coatings against Marine Fouling: A Review. *Polymers* (*Basel*), 13:173.

https://doi.org/10.3390/polym13020173

3. Angell P, Urbanic K, 2000, Sulphate-reducing Bacterial Activity as a Parameter to Predict Localized Corrosion of Stainless Alloys. *Corro Sci*, 42:897–912.

https://doi.org/10.1016/s0010-938x(99)00116-x

4. Veerachamy S, Yarlagadda T, Manivasagam G, *et al.*, 2014, Bacterial Adherence and Biofilm Formation on Medical Implants: A Review. *Proc Inst Mech Eng Part H*, 228:1083–99.

https://doi.org/10.1177/0954411914556137

5. Cloutier M, Mantovani D, Rosei F, 2015, Antibacterial Coatings: Challenges, Perspectives, and Opportunities. *Trends Biotechnol*, 33:637–52.

https://doi.org/10.1016/j.tibtech.2015.09.002

6. Bandara CD, Singh S, Afara IO, *et al.*, 2017, Bactericidal Effects of Natural Nanotopography of Dragonfly Wing on *Escherichia coli*. *ACS Appl Mater Interfaces*, 9:6746–60.

https://doi.org/10.1021/acsami.6b13666

7. Ivanova EP, Hasan J, Webb HK, *et al*., 2012, Natural Bactericidal Surfaces: Mechanical Rupture of *Pseudomonas aeruginosa* Cells by Cicada Wings. *Small*, 8:2489–94.

https://doi.org/10.1002/smll.201200528

8. Kazemzadeh-Narbat M, Lai BF, Ding C, *et al.*, 2013, Multilayered Coating on Titanium for Controlled Release of Antimicrobial Peptides for the Prevention of Implant-associated Infections. *Biomaterials*, 34:5969–77.

https://doi.org/10.1016/j.biomaterials.2013.04.036

9. Park S, Kim HH, Bin Yang S, *et al.*, 2018, A Polysaccharide-Based Antibacterial Coating with Improved Durability for Clear Overlay Appliances. *ACS Appl Mater Interfaces*, 10:17714–21.

https://doi.org/10.1021/acsami.8b04433

10. Peng L, Chang L, Liu X, *et al.*, 2017, Antibacterial Property of a Polyethylene Glycol-Grafted Dental Material. *ACS Appl Mater Interfaces*, 9:17688–692.

https://doi.org/10.1021/acsami.7b05284

11. Zhao Q, Liu C, Su X, *et al.*, 2013, Antibacterial Characteristics of Electroless Plating Ni-P-TiO$_2$ Coatings. *Appl Surf Sci*, 274:101–4.

https://doi.org/10.1016/j.apsusc.2013.02.112

12. Dreyer DR, Park S, Bielawski CW, *et al*., 2010, The Chemistry of Graphene Oxide. *Chem Soc Rev*, 39:228–40.

https://doi.org/10.1039/b917103g

13. Baek SH, Roh J, Park CY, *et al.*, 2020, Cu-nanoflower Decorated Gold Nanoparticles-graphene Oxide Nanofiber as Electrochemical Biosensor for Glucose Detection. *Mater Sci Eng C Mater*, 107:110273.

https://doi.org/10.1016/j.msec.2019.110273

14. Singh V, Kumar V, Kashyap S, *et al.*, 2019, Graphene Oxide Synergistically Enhances Antibiotic Efficacy in Vancomycin-Resistant *Staphylococcus aureus*. *ACS Appl Bio Mater*, 2:1148–57.

https://doi.org/10.1021/acsabm.8b00757

15. Kuila T, Mishra AK, Khanra P, *et al.*, 2013, Recent Advances in the Efficient Reduction of Graphene Oxide and its Application as Energy Storage Electrode Materials. *Nanoscale*, 5:52–71.

https://doi.org/10.1039/c2nr32703a

16. Shih CJ, Lin S, Sharma R, *et al*., 2013, Understanding the pH-dependent Behavior of Graphene Oxide Aqueous Solutions: A Comparative Experimental and Molecular Dynamics Simulation Study. *Langmuir*, 28:235–41.

17. Hu W, Peng C, Luo W, *et al*., 2010, Graphene-Based Antibacterial Paper, *ACS Nano* 4:4317–23.

https://doi.org/10.1021/nn101097v.

18. Akhavan O, Ghaderi E, 2010, Toxicity of Graphene and Graphene Oxide Nanowalls Against Bacteria. *ACS Nano*, 4:5731–6.

https://doi.org/10.1021/nn101390x

19. Ahmed F, Rodrigues DF, 2013, Investigation of Acute Effects of Graphene Oxide on Wastewater Microbial Community: A Case Study. *J Hazard Mater*, 256:33–9.

https://doi.org/10.1016/j.jhazmat.2013.03.064

20. Carpio IE, Santos CM, Wei X, *et al.*, 2012, Toxicity of a Polymer-graphene Oxide Composite Against Bacterial Planktonic Cells, Biofilms, and Mammalian Cells. *Nanoscale*, 4:4746–56.

https://doi.org/10.1039/c2nr30774j

21. Zou X, Zhang L, Wang Z, *et al.*, 2016, Mechanisms of the Antimicrobial Activities of Graphene Materials. *J Am Chem Soc*, 138:2064–77.

https://doi.org/10.1021/jacs.5b11411

22. Tu Y, Lv M, Xiu P, *et al.*, 2013, Destructive Extraction of Phospholipids from *Escherichia coli* Membranes by Graphene Nanosheets. *Nat Nanotechnol*, 8:594–601.

https://doi.org/10.1038/nnano.2013.125

23. Konwar A, Kalita S, Kotoky J, *et al.*, 2016, Chitosan-Iron Oxide Coated Graphene Oxide Nanocomposite Hydrogel: A Robust and Soft Antimicrobial Biofilm. *ACS Appl Mater Interfaces*, 8:20625–34.

https://doi.org/10.1021/acsami.6b07510

24. Liu Y, Wen J, Gao Y, *et al.*, 2018, Antibacterial Graphene Oxide Coatings on Polymer Substrate. *Appl Surf Sci*, 436:624–30.
https://doi.org/10.1016/j.apsusc.2017.12.006

25. Zhao Z, Meng F, Tang J, *et al.*, 2019, A Novel Method of Fabricating an Antibacterial Aluminum-matrix Composite Coating Doped Graphene/Silver-nanoparticles. *Mater Lett*, 245:211–4.
https://doi.org/10.1016/j.matlet.2019.02.121

26. Goh GL, Zhang H, Chong TH, *et al.*, 2021, 3D Printing of Multilayered and Multimaterial Electronics: A Review. *Adv Electron Mater*, 2021:2100445.
https://doi.org/10.1002/aelm.202100445

27. Mahmood MA, Banica A, Ristoscu C, *et al.*, 2021, Laser Coatings via State-of-the-Art Additive Manufacturing: A Review. *Coatings*, 11:296.
https://doi.org/10.3390/coatings11030296

28. Saengchairat N, Tran T, Chua CK, 2017, A Review: Additive Manufacturing for Active Electronic Components. *Virtual Phys Prototype*, 12:31–46.
https://doi.org/10.1080/17452759.2016.1253181

29. Shuai CJ, Yang ML, Deng F, *et al.*, 2020, Forming Quality, Mechanical Properties, and Anti-inflammatory Activity of Additive Manufactured Zn-Nd Alloy. *J Zhejiang Univ A*, 21:876–91.
https://doi.org/10.1631/jzus.A2000186

30. Veres J, Bringans RD, Chow EM, *et al.*, 2016, Additive Manufacturing for Electronics "Beyond Moore". San Francisco, CA, USA: Proceedings of 2016 IEEE International Electron Devices Meeting, p25-6.

31. Choe YE, Kim GH, 2020, A PCL/Cellulose Coil-shaped Scaffoldviaa Modified Electrohydrodynamic Jetting Process. *Virtual Phys Prototype*, 15:403–16.
https://doi.org/10.1080/17452759.2020.1808269

32. Goh GL, Agarwala S, Yeong WY, 2018, High Resolution Aerosol Jet Printing of Conductive Ink for Stretchable Electronics. Proceedings of the 3rd International Conference on Progress in Additive Manufacturing, p109–14.

33. Goh GL, Tay MF, Lee JM, *et al.*, 2021, Potential of Printed Electrodes for Electrochemical Impedance Spectroscopy (EIS): Toward Membrane Fouling Detection. *Adv Electron Mater*, 2021:2100043.
https://doi.org/10.1002/aelm.202100043

34. Wang Z, Zhang G, Huang H, *et al.*, 2021, The Self-induced Electric-field-driven Jet Printing for Fabricating Ultrafine Silver Grid Transparent Electrode. *Virtual Phys Prototy*,
16:113–23.
https://doi.org/10.1080/17452759.2020.1823116

35. Ning F, Cong W, Hu Y, *et al.*, 2017, Additive Manufacturing of Carbon Fiber-reinforced Plastic Composites Using Fused Deposition Modeling: Effects of Process Parameters on Tensile Properties. *J Compos Mater*, 51:451–62.
https://doi.org/10.1177/0021998316646169

36. Alemohammad H, Toyserkani E, 2010, Laser-assisted Additive Fabrication of Micro-sized Coatings. *Adv Laser Mater Process*, 2010:735–62.

37. Hirt L, Ihle S, Pan Z, *et al.*, 2016, Template-Free 3D Microprinting of Metals Using a Force-Controlled Nanopipette for Layer-by-Layer Electrodeposition. *Adv Mater*, 28:2311–5.
https://doi.org/10.1002/adma.201504967

38. Jiang W, Shen L, Qiu M, *et al.*, 2018, Preparation of Ni-SiC composite coatings by magnetic field-enhanced jet electrodeposition. *J Alloys Compd*, 762:115–24.
https://doi.org/10.1016/j.jallcom.2018.05.097

39. Qiao GY, Jing TF, Wang N, *et al.*, 2005, High-speed Jet Electrodeposition and Microstructure of Nanocrystalline Ni-Co Alloys. *Electrochim Acta*, 51:85–92.
https://doi.org/10.1016/j.electacta.2005.03.050

40. Shen L, Xu M, Jiang W, *et al.*, 2019, A Novel Superhydrophobic Ni/Nip Coating Fabricated by Magnetic Field Induced Selective Scanning Electrodeposition. *Appl Surf Sci*, 489:25–33.
https://doi.org/10.1016/j.apsusc.2019.05.335

41. Xu M, Shen L, Jiang W, *et al.*, 2019, Fabrication of Ni-SiC Superhydrophilic Surface by Magnetic Field-assisted Scanning Electrodeposition. *J Alloys Compd*, 799:224–30.
https://doi.org/10.1016/j.jallcom.2019.05.339

42. Ji L, Chen F, Huang H, *et al.*, 2018, Preparation of Nickel-Graphene Composites by Jet Electrodeposition and the Influence of Graphene Oxide Concentration on the Morphologies and Properties. *Surf Coat Technol*, 351:212–9.
https://doi.org/10.1016/j.surfcoat.2018.07.083

43. Arghavanian R, Bostani B, Parvini-Ahmadi N, *et al.*, 2014, Field-enhanced Co-electrodeposition of Zirconia Particles with a Magnetic Shell During Ni Electrodeposition. *Surf Coat Technol*, 258:1171–5.
https://doi.org/10.1016/j.surfcoat.2014.07.015

44. Jena G, Anandkumar B, Sofia S, *et al.*, 2020, Fabrication of Silanized GO Hybrid Coating on 316L SS with Enhanced Corrosion Resistance and Antibacterial Properties for Marine Applications. *Surf Coat Technol*, 402:126295.
https://doi.org/10.1016/j.surfcoat.2020.126295

45. Jena G, Vanithakumari SC, Polaki SR, *et al.*, 2019, Electrophoretically Deposited Graphene Oxide-polymer Bilayer Coating on Cu-Ni Alloy with Enhanced Corrosion Resistance in Simulated Chloride Environment. *J Coat Technol Res*, 16:1317–35.
https://doi.org/10.1007/s11998-019-00213-6

46. Gautier N, 1995, Theoretical Study of the Interaction between a Magnetic Nanotip and a Magnetic Surface. *Phys Rev B*, 52:7352–62.
https://doi.org/10.1103/PhysRevB.52.7352

47. Stone HA, Lister JR, Brenner MP, 1999, Drops with Conical Ends in Electric and Magnetic Fields. *Proc R Soc A Math Phys Eng Sci*, 455:329–47.
https://doi.org/10.1098/rspa.1999.0316

48. Pavithra CL, Sarada BV, Rajulapati KV, *et al.*, 2014, A New Electrochemical Approach for the Synthesis of Copper-Graphene Nanocomposite Foils with High Hardness. *Sci Rep*, 4:4049.
https://doi.org/10.1038/srep04049

49. Qiu J, Liu L, Qian S, *et al.*, 2021, Why does Nitrogen-doped Graphene Oxide Lose the Antibacterial Activity? *J Mater Sci Technol*, 62:44–51.
https://doi.org/10.1016/j.jmst.2020.05.051

50. Shuai C, Guo W, Gao C, *et al.*, 2018, An nMgO Containing Scaffold: Antibacterial Activity, Degradation Properties and Cell Responses. *Int J Bioprint*, 4:120.
https://doi.org/10.18063/IJB.v4i1.120

51. Xie B, Zhao MC, Xu R, *et al.*, 2021, Biodegradation, Antibacterial Performance, and Cytocompatibility of a Novel ZK30-Cu-Mn Biomedical Alloy Produced by Selective Laser Melting. *Int J Bioprint*, 7:78–89.
https://doi.org/10.18063/ijb.v7i1.300

52. Park HJ, Kim JY, Kim J, *et al.*, 2009, Silver-ion-mediated Reactive Oxygen Species Generation Affecting Bactericidal Activity. *Water Res*, 43:1027–32.
https://doi.org/10.1016/j.watres.2008.12.002

53. Chernousova S, Epple M, 2013, Silver as Antibacterial Agent: Ion, Nanoparticle, and Metal. *Angew Chemie Int Ed*, 52:1636–53.
https://doi.org/10.1002/anie.201205923

54. Kedziora A, Speruda M, Krzyzewska E, *et al.*, 2018, Similarities and Differences between Silver Ions and Silver in Nanoforms as Antibacterial Agents. *Int J Mol Sci*, 19:444.
https://doi.org/10.3390/ijms19020444

55. Lemire JA, Harrison JJ, Turner RJ, 2013, Antimicrobial Activity of Metals: Mechanisms, Molecular Targets and Applications. *Nat Rev Microbiol*, 11:371–84.
https://doi.org/10.1038/nrmicro3028

56. Perreault F, de Faria AF, Nejati S, *et al.*, 2015, Antimicrobial Properties of Graphene Oxide Nanosheets: Why Size Matters. *ACS Nano*, 9:7226–36.
https://doi.org/10.1021/acsnano.5b02067

57. Chung H, Kim MJ, Ko K, *et al.*, 2015, Effects of Graphene Oxides on Soil Enzyme Activity and Microbial Biomass. *Sci Total Environ*, 514:307–13.
https://doi.org/10.1016/j.scitotenv.2015.01.077

58. Gurunathan S, Han JW, Dayem AA, *et al.*, 2013, Antibacterial Activity of Dithiothreitol Reduced Graphene Oxide. *J Ind Eng Chem*, 19:1280–8.
https://doi.org/10.1016/j.jiec.2012.12.029

59. Das KK, Das SN, Dhundasi SA, 2008, Nickel, its Adverse Health Effects and Oxidative. *Indian J Med Res*, 128:412–25.

60. Abdel-Rahman LH, Abu-Dief AM, Moustafa H, *et al.*, 2020, Design and Nonlinear Optical Properties (NLO) Using DFT Approach of New Cr(III), VO(II), and Ni(II) Chelates Incorporating Tri-dentate Imine Ligand for DNA Interaction, Antimicrobial, Anticancer Activities and Molecular Docking Studies. *Arab J Chem*, 13:649–70.
https://doi.org/10.1016/j.arabjc.2017.07.007

61. Ohtste N, Hirano Y, Yamaguchi K, *et al.*, 2019, Surface Characteristics, Ni ion Release, and Antibacterial Efficacy of Anodized NiTi Alloy Using HNO$_3$ Electrolyte of Various Concentrations. *Appl Surf Sci*, 492:785–91.
https://doi.org/10.1016/j.apsusc.2019.06.243

62. Vanithakumari SC, Jena G, Sofia S, *et al.*, 2020, Fabrication of Superhydrophobic Titanium Surfaces with Superior Antibacterial Properties Using Graphene Oxide and Silanized Silica Nanoparticles. *Surf Coat Technol*, 400:126074.
https://doi.org/10.1016/j.surfcoat.2020.126074

63. Liu S, Zeng TH, Hofmann M, *et al.*, 2011, Antibacterial Activity of Graphite, Graphite Oxide, Graphene Oxide, and Reduced Graphene Oxide: Membrane and Oxidative Stress. *ACS Nano*, 5:6971–80.
https://doi.org/10.1021/nn202451x

64. Salas E C, Sun Z, Luttge A, *et al.*, 2010, Reduction of Graphene Oxide via Bacterial Respiration. *ACS Nano*, 4:4852–6.
https://doi.org/10.1021/nn101081t

65. Panda S, Rout TK, Prusty AD, *et al.*, 2018, Electron Transfer Directed Antibacterial Properties of Graphene Oxide on Metals. *Adv Mater*, 30:1702149.
https://doi.org/10.1002/adma.201702149

66. Qiu J, Wang D, Geng H, *et al.*, 2017, How Oxygen-Containing Groups on Graphene Influence the Antibacterial Behaviors.

Adv Mater Interfaces, 4:1700228.
https://doi.org/10.1002/admi.201700228

67. Pieper H, Chercheja S, Eigler S, *et al.*, 2016, Endoperoxides Revealed as Origin of the Toxicity of Graphene Oxide. *Angew Chem Int Edi*, 55:405–7.
https://doi.org/10.1002/anie.201507070

68. Zhao J, Wang Z, White JC, *et al.*, 2014, Graphene in the Aquatic Environment: Adsorption, Dispersion, Toxicity and Transformation. *Environ Sci Technol*, 48:9995–10009.
https://doi.org/10.1021/es5022679

69. Wang G, Feng H, Gao A, *et al.*, 2016, Extracellular Electron Transfer from Aerobic Bacteria to Au-Loaded TiO$_2$ Semiconductor without Light: A New Bacteria-Killing Mechanism Other than Localized Surface Plasmon Resonance or Microbial Fuel Cells. *ACS Appl Mater Interfaces*, 8:24509–16.
https://doi.org/10.1021/acsami.6b10052

70. Hassan RY, Wollenberger U, 2016, Mediated Bioelectrochemical System for Biosensing the Cell Viability of *Staphylococcus aureus*. *Ana Bioanal Chem*, 408:579–87.
https://doi.org/10.1007/s00216-015-9134-z

Publisher's note

Whioce Publishing remains neutral with regard to jurisdictional claims in published maps and institutional affiliations